PHYSICAL REVIEW C **111**, 034614 (2025)

Comprehensive Bayesian machine learning approach to estimating the total nuclear capture rate of a negative muon

Hiroki Iwamoto,[1,*] Megumi Niikura,[2] and Rurie Mizuno[3]

[1]*Nuclear Science and Engineering Center, Japan Atomic Energy Agency (JAEA), 2-4 Shirakata,*
Tokai-mura, Naka-gun, Ibaraki 319-1195, Japan
[2]*RIKEN Nishina Center, 2-1, Hirosawa, Wako, Saitama 351-0198, Japan*
[3]*Department of Physics, The University of Tokyo, Hongo, Bunkyo-ku, Tokyo 113-0033, Japan*

(Received 22 October 2024; revised 14 January 2025; accepted 24 February 2025; published 18 March 2025)

Background: A negative muon in the 1*s* orbital of a muonic atom can be captured by a nucleus, leading to subsequent nuclear decay processes. The accurate prediction of total nuclear capture rates, which could be crucial in fields such as geochemistry, nuclear astrophysics, and semiconductor device development, remains challenging with current physics models.
Purpose: This study aims to develop a comprehensive machine learning (ML) model to estimate the total nuclear capture rate of a negative muon, integrating physical information and experimental data within a Bayesian framework.
Methods: The study employs an ML model based on Gaussian process regression, using experimental data with evaluated uncertainties as training data. The model incorporates the Goulard-Primakoff formula as prior information and applies a transfer learning approach to improve estimations, particularly in regions where data on isotopically enriched elements are sparse.
Results: The developed ML model is shown to outperform theoretical physics models in both accuracy and comprehensiveness, with key experiments identified to further refine the model performance.
Conclusions: The estimates generated in this study will be incorporated into muon nuclear data and applied across a variety of research fields.

DOI: 10.1103/PhysRevC.111.034614

I. INTRODUCTION

A negative muon (μ^-) is an elementary particle with an electric charge of $-1e$, a mass of 105.66 MeV, and a mean lifetime of 2.2 µs in vacuum. This particle can occupy an atomic orbital in the same way as an electron, forming a muonic atom. In the 1*s* orbital, the muon either decays or interacts with the nucleus, leading to a process known as muon nuclear capture. When captured by a nucleus with mass number A and atomic number Z, a compound nucleus $(A, Z-1)^*$ is formed, emitting a muon neutrino (ν_μ):

$$\mu^- + (A, Z) \rightarrow (A, Z-1)^* + \nu_\mu, \qquad (1)$$

where the asterisk "*" denotes an excited state. This interaction has the potential to be of crucial importance in research areas such as geochemistry, nuclear astrophysics, and semiconductor device development [1–9]. In light of the potential of muon-induced reactions in these research fields, we are developing nuclear data on negative muon-induced reactions (referred to as muon nuclear data) [10]. Among these data, the total nuclear capture rate is essential for calculating subsequent decay processes following muon capture. Accurately determining this rate is vital for applications related to muon-induced reactions.

The Goulard-Primakoff formula [11] is a well-known method for comprehensively calculating total nuclear capture rates. Despite its widespread use in Monte Carlo particle transport simulations such as PHITS [12], FLUKA [13], and GEANT4 [14], the formula often fails to reproduce experimental values accurately, indicating the need for a new estimation model [15]. Various physics models have been proposed to address this challenge [16–23]. These include the model proposed by Chiang *et al.* [18] based on the local density approximation (hereafter referred to as the Chiang model); the model by Zinner *et al.* [21], which uses the random phase approximation (RPA) based on single-particle states generated by a Woods-Saxon potential (referred to as the Zinner model); and the model by Marketin *et al.* [22], which employs relativistic proton-neutron quasiparticle RPA (*pn*-RQRPA) (referred to as the Marketin model). However, achieving comprehensive accuracy remains a significant hurdle.

In recent years, machine learning (ML) models have been increasingly applied in nuclear physics to effectively address the limitations of traditional physics-based models (see Ref. [24] and references therein). Although ML models lack the inherent ability to explain physical phenomena, their

---

[*] Contact author: iwamoto.hiroki@jaea.go.jp

appropriate use is expected to improve estimation accuracy and advance the theoretical understanding of nuclear reaction mechanisms.

In this paper, we present a comprehensive ML model to estimate the total nuclear capture rate of a negative muon. The model employs a Gaussian process (GP) regression model, as detailed in Refs. [25–27]. The GP regression, based on Bayesian statistics, is particularly suited for handling complex datasets with uncertainties. The ML model uses experimental data with evaluated uncertainties as training data. Extensive measurements of total nuclear capture rates were conducted from the 1960s through the 1980s [28–71], and recent studies have added to this data [72–79], but data for isotopically enriched elements remain limited. This scarcity makes it challenging to comprehensively estimate total nuclear capture rates. To address this issue, we employ a transfer learning approach as described by Iwamoto *et al.* [25], which enables estimation even in data-sparse regions. Additionally, our ML model incorporates the Goulard-Primakoff formula as prior information for the GPs. By integrating this physical insights with experimental data within a Bayesian framework, we achieve estimations supported by both experimental evidence and theoretical understanding.

In Sec. II, we introduce our ML model and estimation process for the total nuclear capture rates. In Sec. III, we present the estimated rates and discuss them, comparing our results with experimental data and calculations obtained using the Goulard-Primakoff formula, as well as other physics models (i.e., the Chiang, Zinner, and Marketin models). We then demonstrate that our ML model outperforms these physics models in both accuracy and comprehensiveness, while identifying key experiments that could further refine model performance. Finally, in Sec. IV, we provide a summary of the study and offer suggestions for future research.

II. MODEL

Figure 1 shows a schematic representation of the estimation process of the developed ML model. If abundant experimental data are available, a straightforward approach can be adopted to learn from the data and estimate the quantities of interest. However, in the present case, this approach cannot be applied directly due to the limited experimental data for enriched isotopes. To address this limitation, the estimation process was divided into two subprocesses: Process A and Process B. In Process A, the total nuclear capture rates of natural composition elements, for which experimental data are relatively abundant, were estimated. In Process B, the capture rate ratios of enriched isotopes relative to the natural composition elements estimated in Process A were estimated. Finally, comprehensive total nuclear capture rates for isotopic nuclides were derived from the results obtained in these two processes. By employing this partitioned approach, it becomes possible to estimate total nuclear capture rates for any element through Process A and to systematically identify trends in the capture rates of isotopes for specific elements through Process B.

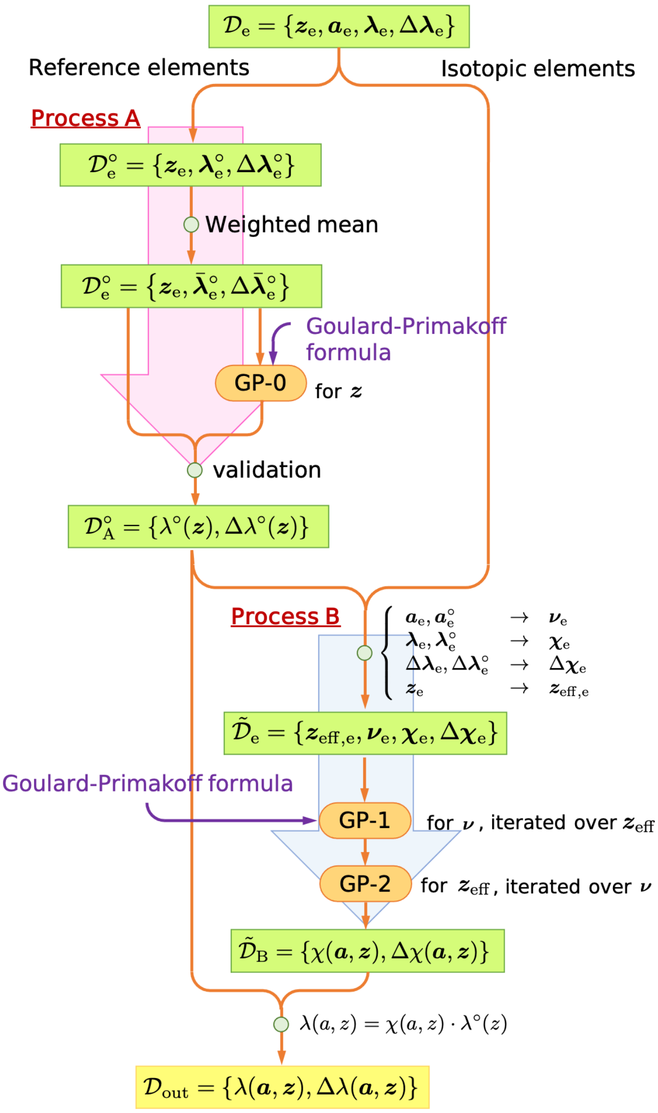

FIG. 1. Estimation process of the developed ML model.

The training set $\mathcal{D}_\mathrm{e}$ was constructed using previously published literature values [28–78] along with recently acquired Si data [79], obtained from the J-PARC muon science establishment, MUSE [80].

A. Process A

In Process A, we compile a dataset of total nuclear capture rates $\mathcal{D}^\circ_\mathrm{e} = \{z_\mathrm{e}, \boldsymbol{\lambda}^\circ_\mathrm{e}, \Delta\boldsymbol{\lambda}^\circ_\mathrm{e}\}$ from the experimental data. z_e is a vector of atomic numbers z, while $\boldsymbol{\lambda}^\circ_\mathrm{e}$ and $\Delta\boldsymbol{\lambda}^\circ_\mathrm{e}$ denote vectors of experimental total nuclear capture rates and their respective 1σ uncertainties. This dataset primarily includes natural composition elements; additionally, isotopically enriched and artificial elements like ^{7}Li and ^{237}Np are also included for comprehensive estimation, referred to as "reference elements." The superscripted circle "$\circ$" indicates reference element. The GP module used in this process is referred to as "GP-0." In principle, individual experimental data could be used as the training dataset. However, in the presence of outliers, GP-0 has the potential to overfit the experimental data. To minimize this possibility, we employed the weighted mean of the experimental data for each reference element in the GP-0 training dataset. Furthermore, as previously noted by Suzuki *et al.* [69], the total nuclear capture rate of odd-Z nuclei is systematically larger than that of adjacent even-Z nuclei. Consequently, to mitigate the risk of overfitting due to this systematic difference, separate regressions were conducted for the odd-Z and even-Z nuclei. Based on the regression results, we confirmed that GP-0 does not exhibit overfitting.

The weighted mean for a reference element $\bar{\lambda}^\circ_{\mathrm{e}}$ is calculated as

$$\bar{\lambda}^\circ_{\mathrm{e}} = \frac{\sum_i w_i \lambda^\circ_{\mathrm{e},i}}{\sum_i w_i}, \tag{2}$$

where $\lambda^\circ_{\mathrm{e},i}$ and $w_i (= 1/\Delta\lambda^\circ_{\mathrm{e},i})$ indicate the ith experimental value and its weight, respectively. The uncertainty of $\bar{\lambda}^\circ_{\mathrm{e}}$, $\Delta\bar{\lambda}^\circ_{\mathrm{e}}$, is calculated using a widely accepted nuclear data evaluation method [81,82] in which the larger of the internal and external uncertainties is adopted:

$$\Delta\bar{\lambda}^\circ_{\mathrm{e}} = \max\,(\delta_{\mathrm{int}}, \delta_{\mathrm{ext}}), \tag{3}$$

where δ_{int} and δ_{ext} denote the internal and external uncertainties, expressed as

$$\delta_{\mathrm{int}} = \frac{1}{\sqrt{\sum_i w_i}}, \tag{4}$$

and

$$\delta_{\mathrm{ext}} = \frac{\sqrt{\sum_i w_i (\lambda^\circ_{\mathrm{e},i} - \bar{\lambda}^\circ_{\mathrm{e}})^2}}{\sqrt{df \sum_i w_i}}, \tag{5}$$

respectively. Here, df denotes the degree of freedom.

In GP-0, we assume that $\boldsymbol{\lambda}^\circ$, which is a function of $\boldsymbol{z}$, follows a GP with mean $\boldsymbol{\mu}$ and covariance $\mathbf{K}$, i.e., $\boldsymbol{\lambda}^\circ \sim \mathcal{GP}(\boldsymbol{\mu}, \mathbf{K})$, then the observed values $\boldsymbol{\lambda}^\circ$ at $\boldsymbol{z}_*$ (denoted $\boldsymbol{\lambda}^\circ_*$), given $\mathcal{D}^\circ_{\mathrm{e}}$, follow a multivariate normal distribution:

$$\boldsymbol{\lambda}^\circ_* | \mathcal{D}^\circ_{\mathrm{e}} \sim \mathcal{N}(\boldsymbol{m}^\circ_*, \boldsymbol{\Sigma}^\circ_*), \tag{6}$$

where

$$\boldsymbol{m}^\circ_* = \boldsymbol{\mu}_* + \mathbf{K}^\top_{*,\mathrm{e}} \mathbf{K}^{-1}_{\mathrm{e,e}} (\boldsymbol{\lambda}^\circ_{\mathrm{e}} - \boldsymbol{\mu}_{\mathrm{e}}), \tag{7}$$

$$\boldsymbol{\Sigma}^\circ_* = \mathbf{K}_{*,*} - \mathbf{K}^\top_{*,\mathrm{e}} \mathbf{K}^{-1}_{\mathrm{e,e}} \mathbf{K}_{\mathrm{e},*}. \tag{8}$$

In these equations, $\mathbf{K}_{*,\mathrm{e}}$ (equivalent to $\mathbf{K}_{\mathrm{e},*}$) is defined as $\kappa(\boldsymbol{z}_*, \boldsymbol{z}_{\mathrm{e}})$, $\mathbf{K}_{\mathrm{e,e}}$ as $\kappa(\boldsymbol{z}_{\mathrm{e}}, \boldsymbol{z}_{\mathrm{e}}) + \mathrm{diag}((\Delta\boldsymbol{\lambda}^\circ_{\mathrm{e}})^2)$, and $\mathbf{K}_{*,*}$ as $\kappa(\boldsymbol{z}_*, \boldsymbol{z}_*)$, where κ represents a kernel function. The kernel function can take various forms. In this study, we used the Matérn 3/2 kernel because it has a simple functional form, is robust against overfitting, and has been widely applied in various fields of research.

The Matérn 3/2 kernel is expressed using the Euclidean distance between two data points x and x', $r \equiv \|x - x'\|$, as

$$\kappa_{\mathrm{M3}}(x, x' | \boldsymbol{\theta}) = \sigma^2 \left(1 + \frac{\sqrt{3}r}{\ell}\right) \exp\left(-\frac{\sqrt{3}r}{\ell}\right), \tag{9}$$

where $\boldsymbol{\theta}$ $[=(\sigma, \ell)]$ is a set of the hyperparameters. The optimal hyperparameter set $\boldsymbol{\theta}_{\mathrm{opt}}$ is determined by maximizing the marginal likelihood, which is expressed as

$$\boldsymbol{\theta}_{\mathrm{opt}} = \underset{\boldsymbol{\theta}}{\mathrm{argmax}}\, \mathcal{L}(\boldsymbol{\theta}). \tag{10}$$

Here, $\mathcal{L}(\boldsymbol{\theta})$ denotes the log-marginal likelihood and is given by

$$\mathcal{L}(\boldsymbol{\theta}) \propto -\ln|\mathbf{K}_{\mathrm{e,e}}| - (\boldsymbol{\lambda}^\circ_{\mathrm{e}} - \boldsymbol{\mu}_{\mathrm{e}})^\top \mathbf{K}^{-1}_{\mathrm{e,e}} (\boldsymbol{\lambda}^\circ_{\mathrm{e}} - \boldsymbol{\mu}_{\mathrm{e}}) + \text{const.} \tag{11}$$

To solve this maximization problem efficiently, the gradient descent method was employed, and L-BFGS-B [83] was used as the solver. This approach requires the gradient of $\mathcal{L}$ with respect to $\theta \in \boldsymbol{\theta}$, which is expressed as

$$\begin{aligned} \frac{\partial \mathcal{L}}{\partial \theta} &= -\mathrm{tr}\left(\mathbf{K}^{-1}_{\mathrm{e,e}} \frac{\partial \mathbf{K}_{\mathrm{e,e}}}{\partial \theta}\right) \\ &\quad + \left\{\mathbf{K}^{-1}_{\mathrm{e,e}} (\boldsymbol{\lambda}^\circ_{\mathrm{e}} - \boldsymbol{\mu}_{\mathrm{e}})\right\}^\top \frac{\partial \mathbf{K}_{\mathrm{e,e}}}{\partial \theta} \left\{\mathbf{K}^{-1}_{\mathrm{e,e}} (\boldsymbol{\lambda}^\circ_{\mathrm{e}} - \boldsymbol{\mu}_{\mathrm{e}})\right\}. \end{aligned} \tag{12}$$

In this expression, $\partial \mathbf{K}_{\mathrm{e,e}} / \partial \theta$ is equivalent to $\partial\kappa/\partial\sigma$ and $\partial\kappa/\partial\ell$. For the Matérn 3/2 kernel, these gradients are given as

$$\frac{\partial \kappa_{\mathrm{M3}}}{\partial \sigma} = 2\sigma^2 \left(1 + \frac{\sqrt{3}r}{\ell}\right) \exp\left(-\frac{\sqrt{3}r}{\ell}\right), \tag{13}$$

and

$$\frac{\partial \kappa_{\mathrm{M3}}}{\partial \ell} = \frac{3\sigma^2 r^2}{\ell^3} \exp\left(-\frac{\sqrt{3}r}{\ell}\right). \tag{14}$$

The mean functions $\boldsymbol{\mu}_*$ and $\boldsymbol{\mu}_{\mathrm{e}}$ in Eqs. (7), (11), and (12), which represent the prior means of $\boldsymbol{\lambda}^\circ$, are calculated using the Goulard-Primakoff formula:

$$\begin{aligned} \lambda_{\mathrm{Gou.Pri.}}(a, z) &= z^4_{\mathrm{eff}}\, g_1 \left\{1 + g_2 \frac{a}{2z} - g_3 \frac{a - 2z}{2z} \right. \\ &\quad \left. - g_4 \left(\frac{a - z}{2a} + \frac{a - 2z}{8az}\right)\right\}, \end{aligned} \tag{15}$$

where a denotes mass number; z_{eff} represents the effective charge post-muon capture by the nucleus. We utilize a simple form for z_{eff} to align with theoretical values [84]:

$$z_{\mathrm{eff}} = q_0 z^3 + q_1 z^2 + q_2 z + q_3, \tag{16}$$

with coefficients $q_0 = 4.316 \times 10^{-5}$, $q_1 = -1.070 \times 10^{-2}$, $q_2 = 9.978 \times 10^{-1}$, and $q_3 = 1.326 \times 10^{-1}$. The fitting parameters g_1 to g_4 are taken from the TRIUMF data [69] (i.e., $g_1 = 261$, $g_2 = -0.04$, $g_3 = -0.26$, and $g_4 = 3.24$). For natural composition elements, we assume that a is given as the weighted mean mass number, considering the natural composition for elements with z (e.g., $a = 28.11$ for Si).

B. Process B

Similar to the total nuclear capture rate, if abundant experimental data on the capture rate ratio are available for Z and A, a straightforward approach using a single GP model with both Z and A as variables simultaneously could be applied.

However, in the present case, the lack of experimental data makes it challenging to implement this approach. To address this limitation, Process B employs two combined GP modules, referred to as "GP-1" and "GP-2," as proposed by Iwamoto *et al.* [25]. This method, which is a form of transfer learning, enables comprehensive estimations for various nuclides, even in regions of Z and A with no or limited training data, by leveraging estimates from regions where experimental data are available.

To execute this process, we introduce the capture rate ratio χ and its uncertainty $\Delta\chi$ with respect to the reference element, Additionally, the neutron number difference from the reference element, ν, was defined as an explanatory variable for χ instead of the mass number a, to identify trends in deviations relative to the reference element's capture rate, expressed as

$$\nu \equiv a - a^{\circ}, \tag{17}$$

where a° denotes the mass number of the reference element. Furthermore, to mitigate the risk of overfitting caused by abrupt changes in χ of lighter elements, z_{eff}, which exhibits less variation in capture rate compared to z, was used as another explanatory variable instead of z.

A dataset of isotopic nuclear capture rate ratios, $\tilde{\mathcal{D}}_{\mathrm{e}} = \{\boldsymbol{z}_{\mathrm{eff,e}}, \boldsymbol{\nu}_{\mathrm{e}}, \boldsymbol{\chi}_{\mathrm{e}}, \Delta\boldsymbol{\chi}_{\mathrm{e}}\}$, was constructed, where $\{\boldsymbol{\chi}_{\mathrm{e}} \mid \chi_{\mathrm{e},i} = \lambda_{\mathrm{e},i}/\lambda^{\circ}_{\mathrm{e}}\}$ and $\{\Delta\boldsymbol{\chi}_{\mathrm{e}} \mid \Delta\chi_{\mathrm{e},i} = \{(\Delta\lambda_{\mathrm{e},i}/\lambda_{\mathrm{e},i})^2 + (\Delta\lambda^{\circ}_{\mathrm{e}}/\lambda^{\circ}_{\mathrm{e}})^2\}^{1/2}\chi_{\mathrm{e},i}\}$. From the constructed training dataset, GP-1 derives $\boldsymbol{\chi}$ as a function of $\boldsymbol{\nu}$. GP-2 learns from the χ values obtained by GP-1 and determines $\boldsymbol{\chi}$ as a function of $\boldsymbol{z}_{\mathrm{eff}}$ for any ν. This combined method provides χ values for any z_{eff} and ν [or equivalently, any z and a based on Eqs. (16) and (17)].

Since the training dataset in Process B is very small, the risk of overfitting due to outliers is considered low. Therefore, in this process, the experimental values χ_{e} were used directly as training data, rather than employing weighted means as was done in Process A.

In GP-1, we assume that $\boldsymbol{\chi}$ is a function of $\boldsymbol{\nu}$ and $\boldsymbol{\chi} \sim \mathcal{GP}(\boldsymbol{\mu}, \mathbf{K})$, then the observed values $\boldsymbol{\chi}$ at $\boldsymbol{\nu}_*$ (denoted as $\boldsymbol{\chi}_*$), given $\tilde{\mathcal{D}}_{\mathrm{e}}$, are given by

$$\boldsymbol{\chi}_* | \tilde{\mathcal{D}}_{\mathrm{e}} \sim \mathcal{N}(\boldsymbol{m}_*, \boldsymbol{\Sigma}_*), \tag{18}$$

where

$$\boldsymbol{m}_* = \boldsymbol{\mu}_* + \mathbf{K}_{*,\mathrm{e}}^{\top}\mathbf{K}_{\mathrm{e,e}}^{-1}(\boldsymbol{\chi}_{\mathrm{e}} - \boldsymbol{\mu}_{\mathrm{e}}), \tag{19}$$

$$\boldsymbol{\Sigma}_* = \mathbf{K}_{*,*} - \mathbf{K}_{*,\mathrm{e}}^{\top}\mathbf{K}_{\mathrm{e,e}}^{-1}\mathbf{K}_{\mathrm{e},*}. \tag{20}$$

For the kernel functions $\mathbf{K}_{*,\mathrm{e}}$ (equivalent to $\mathbf{K}_{\mathrm{e},*}$) defined as $\kappa(\boldsymbol{\nu}_*, \boldsymbol{\nu}_{\mathrm{e}})$, $\mathbf{K}_{\mathrm{e,e}}$ as $\kappa(\boldsymbol{\nu}_{\mathrm{e}}, \boldsymbol{\nu}_{\mathrm{e}}) + \mathrm{diag}((\Delta\boldsymbol{\chi}_{\mathrm{e}})^2)$, and $\mathbf{K}_{*,*}$ as $\kappa(\boldsymbol{\nu}_*, \boldsymbol{\nu}_*)$, we utilized the Matérn 3/2 kernel. The optimization of its hyperparameters was performed using the previously described method. The mean functions $\boldsymbol{\mu}_*$ and $\boldsymbol{\mu}_{\mathrm{e}}$ in Eq. (19), which represent the prior means of $\boldsymbol{\chi}$, are calculated using Eq. (15):

$$\chi_{\mathrm{Gou.Pri.}} = \frac{\lambda_{\mathrm{Gou.Pri.}}(a^{\circ} + \nu, z^{\circ})}{\lambda_{\mathrm{Gou.Pri.}}(a^{\circ}, z^{\circ})}. \tag{21}$$

The above GP-1 calculation is iterated over all z_{eff} values to be calculated.

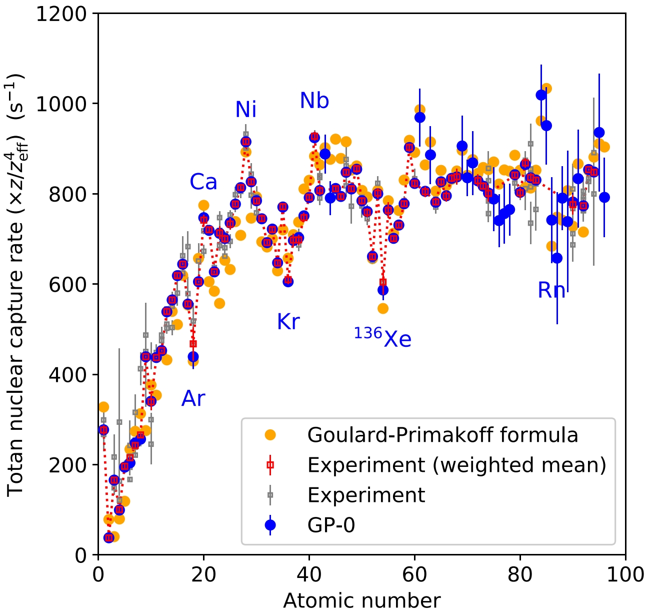

FIG. 2. Total nuclear capture rates for reference elements estimated by GP-0 and the Goulard-Primakoff formula, along with the experimental values and their weighted mean for each element. The respective rates are multiplied by z/z_{eff}^4. The error bar indicates 1σ uncertainty.

In GP-2, we assume that $\boldsymbol{\chi}$ is a function of $\boldsymbol{z}_{\mathrm{eff}}$. Since prior knowledge is already provided in GP-1, no prior knowledge is incorporated here. Typically, in the absence of prior knowledge, a zero-mean GP is assumed for modeling simplicity. Accordingly, in GP-2, a zero-mean GP is also assumed [i.e., $\boldsymbol{\chi} \sim \mathcal{GP}(\mathbf{0}, \mathbf{K})$]. Under this assumption, the observed values of $\boldsymbol{\chi}$ at $\boldsymbol{z}_{**}$ (denoted $\boldsymbol{\chi}_{**}$), given $\tilde{\mathcal{D}}_*$, follow a multivariate normal distribution:

$$\boldsymbol{\chi}_{**} | \tilde{\mathcal{D}}_{\mathrm{e}} \sim \mathcal{N}(\boldsymbol{m}_{**}, \boldsymbol{\Sigma}_{**}), \tag{22}$$

where

$$\boldsymbol{m}_{**} = \mathbf{K}_{**,*}^{\top}\mathbf{K}_{*,*}^{-1}\boldsymbol{\chi}_*, \tag{23}$$

$$\boldsymbol{\Sigma}_{**} = \mathbf{K}_{**,**} - \mathbf{K}_{**,*}^{\top}\mathbf{K}_{*,*}^{-1}\mathbf{K}_{*,**}. \tag{24}$$

For the kernel functions $\mathbf{K}_{**,*}$ (equivalent to $\mathbf{K}_{*,**}$) defined as $\kappa(\boldsymbol{z}_{\mathrm{eff},**}, \boldsymbol{z}_{\mathrm{eff},*})$, $\mathbf{K}_{*,*}$ as $\kappa(\boldsymbol{z}_{\mathrm{eff},*}, \boldsymbol{z}_{\mathrm{eff},*}) + \mathrm{diag}((\Delta\boldsymbol{\chi}_*)^2)$, and $\mathbf{K}_{**,**}$ as $\kappa(\boldsymbol{z}_{\mathrm{eff},**}, \boldsymbol{z}_{\mathrm{eff},**})$, we utilized the Matérn 3/2 kernel. The optimal values of the hyperparameters were obtained using the same method as described above, except that $\boldsymbol{\mu}_{\mathrm{e}}$ in Eqs. (11) and (12) is zero. The above GP-2 calculation is iterated over all ν values to be calculated.

III. RESULTS AND DISCUSSION

A. Total nuclear capture rates for reference elements

Figure 2 shows the total nuclear capture rates for reference elements obtained from the experimental data in Table I, along with the weighted mean rates for each element, accounting for

TABLE I. Experimental data employed in Process A. The values in parentheses represent 1σ experimental uncertainties in the least significant digits.

Elem.	z_e	λ_e° (μs^{-1})
^{1}H	1	0.000420(20) [62], 0.000420(60) [65], 0.000470(29) [66]
^{4}He	2	0.000336(75) [42], 0.000364(46) [47]
^{7}Li	3	0.018(11) [37], 0.0226(12) [57], 0.0181(44) [69]
Be	4	0.018(10) [37], 0.010(2) [28], 0.0059(2) [63], 0.0074(5) [69]
^{11}B	5	0.0218(16) [37], 0.0219(7) [69]
C	6	0.044(10) [28], 0.036(4) [29], 0.0373(11) [30], 0.0361(10) [32], 0.037(7) [33], 0.0397(13) [37], 0.0365(20) [41], 0.0303(7) [43], 0.0376(4) [63], 0.0352(25) [45], 0.0377(7) [67], 0.0388(5) [69]
N	7	0.086(11) [28], 0.065(4) [37], 0.0602(8) [63], 0.0684(8) [67], 0.0693(8) [69]
O	8	0.159(14) [28], 0.098(3) [37], 0.098(5) [43], 0.095(8) [45], 0.1026(6) [69]
F	9	0.254(22) [28], 0.235(10) [34], 0.231(6) [41], 0.229(1) [69]
Ne	10	0.204(10) [38], 0.167(30) [39], 0.30(2) [52], 0.235(5) [63]
Na	11	0.387(15) [28], 0.3772(14) [69]
Mg	12	0.507(20) [28], 0.480(2) [32], 0.52(2) [44], 0.4841(18) [69]
Al	13	0.691(20) [28], 0.662(3) [32], 0.650(15) [34], 0.7054(13) [69]
Si	14	0.777(25) [28], 0.850(3) [32], 0.86(4) [44], 0.8712(18) [69], 0.8786(18) [79], 0.877(6) [79]
P	15	1.05(5) [28], 1.121(5) [32], 1.185(3) [69]
S	16	1.39(9) [28], 1.31(3) [44], 1.34(1) [41], 1.352(3) [69]
Cl	17	1.39(9) [28], 1.333(6) [69], 1.64(8) [31]
Ar	18	1.20(8) [52], 1.41(11) [60]
K	19	1.99(12) [28], 1.849(5) [69]
Ca	20	2.55(5) [28], 2.444(23) [35], 2.529(8) [50], 2.29(5) [56], 2.557(14) [69]
Sc	21	2.711(25) [69]
Ti	22	2.63(6) [28], 2.60(4) [44], 2.590(12) [69]
V	23	3.37(6) [28], 3.24(7) [33], 3.09(5) [44], 3.069(25) [69]
Cr	24	3.24(8) [28], 3.33(6) [44], 3.472(31) [69], 3.444(47) [45]
Mn	25	3.67(8) [28], 3.98(5) [44], 3.857(37) [69]
Fe	26	4.53(10) [28], 4.38(7) [33], 4.40(5) [44], 4.411(24) [69]
Co	27	4.89(9) [33], 4.96(5) [44], 4.940(29) [69]
Ni	28	6.03(14) [28], 5.89(12) [33], 5.83(13) [44], 5.932(41) [69], 5.88(10) [45]
Cu	29	5.79(16) [28], 5.47(20) [34], 5.66(9) [36], 5.67(9) [44], 5.676(37) [69]
Zn	30	5.76(17) [28], 5.5(1) [33], 5.76(5) [44], 5.676(37) [69]
Ga	31	5.70(6) [44]
Ge	32	5.54(6) [44], 5.569(36) [69]
As	33	6.07(7) [44], 6.06(12) [36], 6.104(4) [69]
Se	34	5.70(5) [44], 5.681(37) [69], 5.68(7) [76], 5.59(7) [76]
Br	35	7.07(6) [69]
Kr	36	5.81(10) [76]
Rb	37	6.89(14) [44]
Sr	38	7.25(14) [44], 7.02(14) [69]
Y	39	7.89(11) [36]
Zr	40	8.59(7) [44], 8.66(8) [69]
Nb	41	10.40(14) [36], 10.36(17) [69]
Mo	42	9.09(18) [28], 9.23(7) [44], 9.614(15) [69]
Rh	45	10.01(7) [44]
Pd	46	10.00(7) [44]
Ag	47	11.25(50) [28], 10.86(13) [36], 10.88(14) [44], 10.5(3) [31], 11.07(20) [69]
Cd	48	10.1(5) [28], 10.63(11) [36], 10.61(18) [69], 10.43(31) [76], 10.11(75) [76]
In	49	11.37(13) [36], 11.40(21) [69]
Sn	50	10.5(4) [33], 10.70(14) [36], 10.44(18) [69]
Sb	51	10.49(14) [36], 10.21(20) [69]
Te	52	9.06(11) [44], 9.27(10) [69]
I	53	11.20(11) [36], 11.58(22) [69]
^{136}Xe	54	8.6(4) [73]
Cs	55	10.98(25) [36]
Ba	56	10.18(10) [36], 9.94(16) [69]
La	57	10.71(10) [36]
Ce	58	11.44(11) [36], 11.60(14) [69]

TABLE I. (*Continued.*)

Elem.	z_e	λ_e° (μs^{-1})
Nd	60	12.32(14) [36], 12.50(33) [69]
Sm	62	12.22(17) [36]
Gd	64	12.09(16) [36], 11.82(22) [69]
Tb	65	12.73(13) [36]
Dy	66	12.29(18) [69]
Ho	67	12.95(13) [36]
Er	68	13.04(27) [69]
Hf	72	13.03(21) [36]
Ta	73	12.86(13) [36]
W	74	11.92(30) [28], 13.5(6) [33], 13.07(21) [44], 12.36(24) [69]
Au	79	13.39(11) [36], 13.07(28) [69]
Hg	80	12.74(26) [44], 12.74(26) [69]
Tl	81	12.90(75) [28], 13.83(20) [36], 13.90(31) [69]
Pb	82	11.70(75) [28], 14.5(7) [33], 12.98(10) [36], 13.27(22) [44], 13.45(18) [69], 13.61(10) [36]
Bi	83	12.20(75) [28], 13.26(7) [36], 13.10(18) [69]
^{232}Th	90	13.1(9) [40], 11.1(6) [53], 12.56(5) [61], 11.5(6) [55], 12.4(3) [58]
^{238}U	92	12.4(4) [70], 13.1(5) [48], 12.9(5) [40], 12.8(2) [53], 12.60(4) [61], 12.46(9) [59], 12.50(10) [58], 12.4(4) [64], 12.57(7) [68] 12.62(7) [72]
^{237}Np	93	13.6(2) [59], 13.5(4) [54], 13.96(4) [72], 13.92(4) [71]
^{239}Pu	94	13.1(2.6) [46], 13.9(9) [54], 13.9(2) [59], 14.6(2.0) [51], 13.88(14) [71]

experimental uncertainties, and the analysis results using the Goulard-Primakoff formula, where each value is multiplied by $z/z_{\rm eff}^4$ for visual clarity. In Fig. 3, the upper panel compares the relative differences from GP-0 between estimates from the Goulard-Primakoff formula and the weighted means, while the lower panel compares the 1σ uncertainties between GP-0 and the weighted means. As shown in these figures,

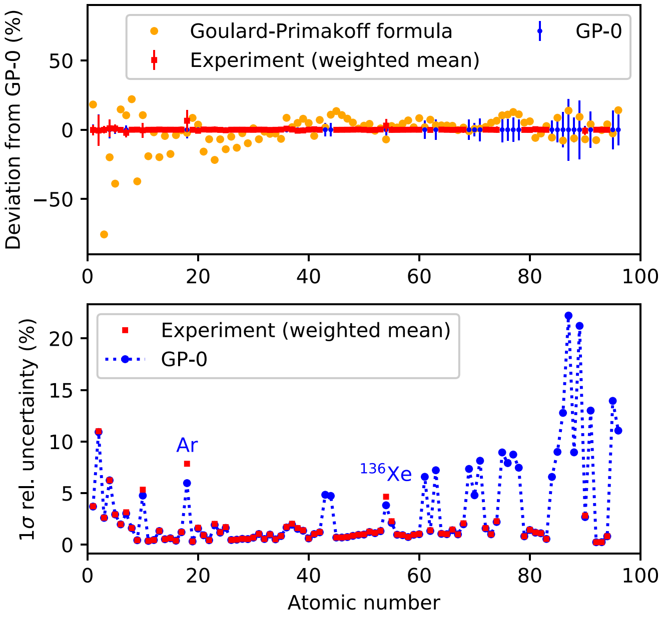

FIG. 3. (upper panel) Relative deviation from GP-0 estimates. The red squares represent the weighted means of the experimental values, while the orange dots indicate estimates from the Goulard-Primakoff formula. (lower panel) 1σ uncertainties estimated using two methods: weighted means of experimental values and GP-0.

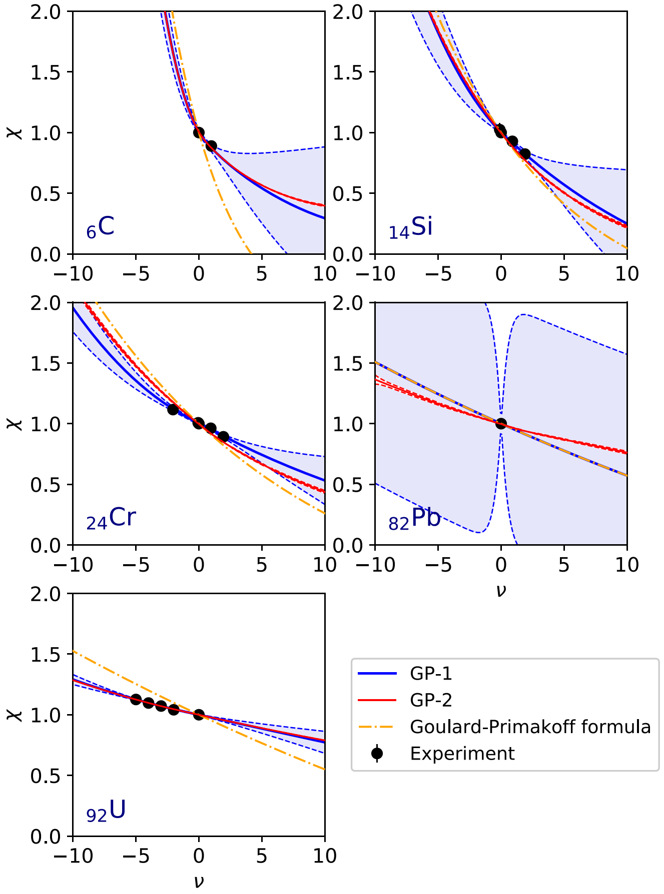

FIG. 4. Capture rate ratios relative to reference elements (C, Si, Cr, Pb, and U) as estimated by GP-1 and GP-2, alongside calculations using the Goulard-Primakoff formula. The blue and red banded lines represent the estimates by GP-1 and GP-2, respectively. The band widths indicate the 1σ uncertainties.

TABLE II. Experimental data employed in Process A. The values in parentheses represent 1σ experimental uncertainties in the least significant digits.

Elem.	$z_{\mathrm{eff,e}}$	a_{e}	ν_{e}	λ_{e} (μs^{-1})
B	4.86	10	−1	0.0265(15) [37], 0.0278(7) [69]
C	5.72	13	0.99	0.0338(4) [67], 0.0376(7) [69]
O	7.49	18	2.00	0.0880(15) [69]
Si	12.12	28	−0.11	0.891(9) [79]
		29	0.89	0.807(6) [79]
		30	1.89	0.714(4) [79]
Ca	16.15	43.8	3.68	1.793(40) [35]
		48	7.88	1.214(8) [75]
Cr	18.51	50	−2.6	3.825(50) [45]
		52	−0.6	3.452(47) [45]
		53	0.94	3.297(45) [45]
		54	1.94	3.057(42) [45]
Ni	20.63	58	−0.78	6.110(105) [45]
		60	1.24	5.562(97) [45]
		62	3.24	4.716(95) [45]
Se	23.38	76	−3.04	6.300(4) [76]
		80	0.96	4.96(7) [76]
		82	2.96	4.37(14) [76]
Kr	24.20	82	−1.89	6.576(17) [76]
		84	0.11	5.75(15) [73]
		86	2.11	5.33(8) [76]
Pd	27.59	104	−2.51	11.1(4) [78]
		105	−1.51	8.8(6) [78]
		106	−0.51	9.9(7) [78]
		108	1.49	8.8(3) [78]
		110	3.49	9.4(6) [78]
Cd	28.15	114	1.57	9.380(14) [76]
		116	3.57	8.86(15) [76]
Xe	29.61	129	−7	11.7(3) [74]
		132	−4	9.4(2) [74]
U	34.97	233	−5	15.8(9) [48], 14.23(15) [58], 14.14(6) [72]
		234	−4	13.79(4) [72]
		235	−3	13.7(4) [70], 14.9(6) [48], 14.7(1.0) [40], 12.9(4) [53], 13.3(2) [59], 13.36(12) [58], 13.58(12) [68], 13.9(4) [70], 13.48(4) [72]
		236	−2	13.09(10) [72]
Pu	35.23	242	3	12.9(2) [59], 12.3(8) [54], 12.90(7) [71]
		244	5	12.40(7) [71]

the Goulard-Primakoff formula approximately captures the trend of experimental values but does not match the weighted means. In contrast, the GP-0 estimates closely align with both weighted means and their 1σ uncertainties, although discrepancies are observed for certain elements (e.g., Ar and ^{136}Xe). These discrepancies are attributed to correlations between elements defined using the kernel function. The kernel function allows GP-0 to estimate the rates even in the regions where no experimental data exist, though the uncertainties in these regions are large (see the lower panel of Fig. 3). It is also worth noting that, in such regions, the GP-0 results are generally in agreement with the Goulard-Primakoff formula within a 1σ uncertainty, which can be attributed to the fact that this formula is used as prior information in GP-0. These large uncertainties can be reduced, based on Bayesian statistics, through new measurements.

Although the values estimated by the weighted mean and GP-0 are nearly identical, since the weighted mean is the more widely used and is recommended for use by the nuclear data community [82], we adopted the weighted mean (or the experimental values themselves if only a single data point exists) for elements where experimental data are available.

B. Total nuclear capture rates for nuclei

Figure 4 illustrates the capture rate ratios of C, Si, Cr, Pb, and Pu relative to their respective reference elements, using GP-1 and GP-2, along with calculations using the Goulard-Primakoff formula. GP-1 was trained using the experimental data in Table I and the isotopic data from Table II. Although isotopic data of ^{35,37}Cl [31], ^{63}Cu [44], ^{88}Sr [44], ^{79,81}Br [49], ^{48}Ti [76], ^{150}Sm [76], and ^{24}Mg [77] are also available,

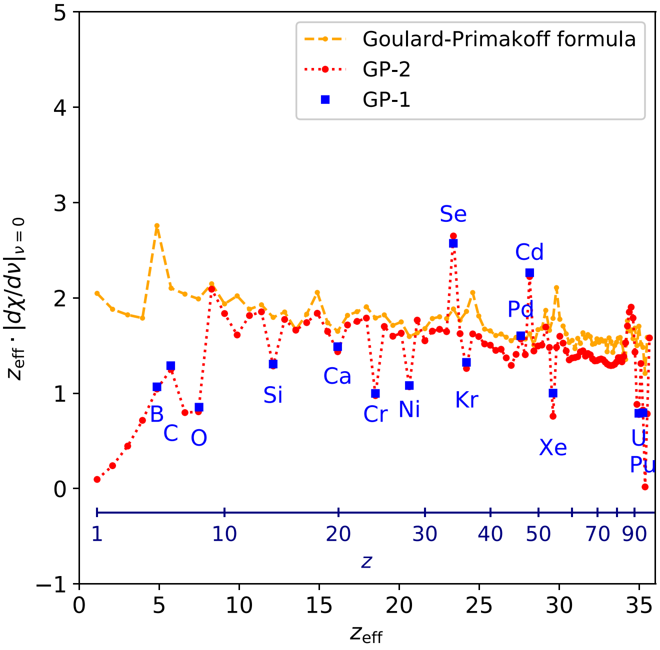

FIG. 5. Absolute values of the differential coefficients of χ with respect to ν at $\nu = 0$, multiplied by $z_{\rm eff}$.

Suzuki *et al.* [69] noted that the accuracy of the data for Cu, Sr, and Br is inadequate, and the data for Cl is questionable. Additionally, the data of ^{48}Ti, ^{150}Sm, and ^{24}Mg produced apparently unnatural results in the regression, despite the absence of clear indications of issues. Consequently, these data were excluded to avoid negatively impacting the capture rate ratio estimation. Figure 5 presents absolute values of the differential coefficients of capture rate ratios at $\nu = 0$, with each value multiplied by $z_{\rm eff}$.

The experimental values exhibit a monotonically decreasing trend with increasing ν (or A) for each Z. Primakoff [16] attributes this trend to the Pauli exclusion principle, and the Goulard-Primakoff formula explains it through the fourth term of Eq. (15). However, the estimated slope is consistently steeper than that observed experimentally, except in the cases of Se and Cd (see Fig. 5). The GP-1 uses the Goulard-Primakoff formula as prior information to estimate the capture rate ratio. Consequently, in the absence of isotopic data as in the case of Pb in Fig. 4, GP-1 estimates are comparable to those derived from the Goulard-Primakoff formula, albeit with considerable uncertainty. In contrast, the GP-2 comprehensively estimates the capture rate ratios based on the results of GP-1 while incorporating data from other elements. As a result, it produces a less steep slope than that estimated by GP-1 (or the Goulard-Primakoff formula) and slightly lower goodness of fit due to the influence of the data from other elements (see the Si and Cr cases in Fig. 4). Therefore, in instances where the data have been systematically measured—specifically for Si, Ca, Cr, Ni, Pd, U, and Pu—the ratios from GP-1, which exhibit as superior goodness of fit, were employed as the estimates for Process B.

Figure 6 shows the total nuclear capture rates for isotopes from H ($z = 1$) to Cm ($z = 96$), obtained from $\lambda(a, z) = \chi(a, z)\lambda^{\circ}(z)$. The generated data can be found in the Supplemental Material [85]. For clarity, odd-Z nuclei are shown in red, while even-Z nuclei are shown in blue. The band widths represent the 1σ uncertainties, accounting for the uncertainty propagation. For lighter nuclei (i.e., H, He, Li, and B), experimental data were adopted for the evaluated values, because GP-2 cannot accommodate abrupt changes in the capture rate ratio due to boundary conditions of ν (e.g., $\nu \geqslant -2$ for ^{4}He). Figure 6 demonstrates that our ML model fits well to the experimental values over a very wide range. For elements without training data in Process A (e.g., Po, Am, and Cm) and for elements with training data but large experimental uncertainties (e.g., Ar and Xe), the uncertainty band width for their isotopes is also large due to the propagation of uncertainties from Process A.

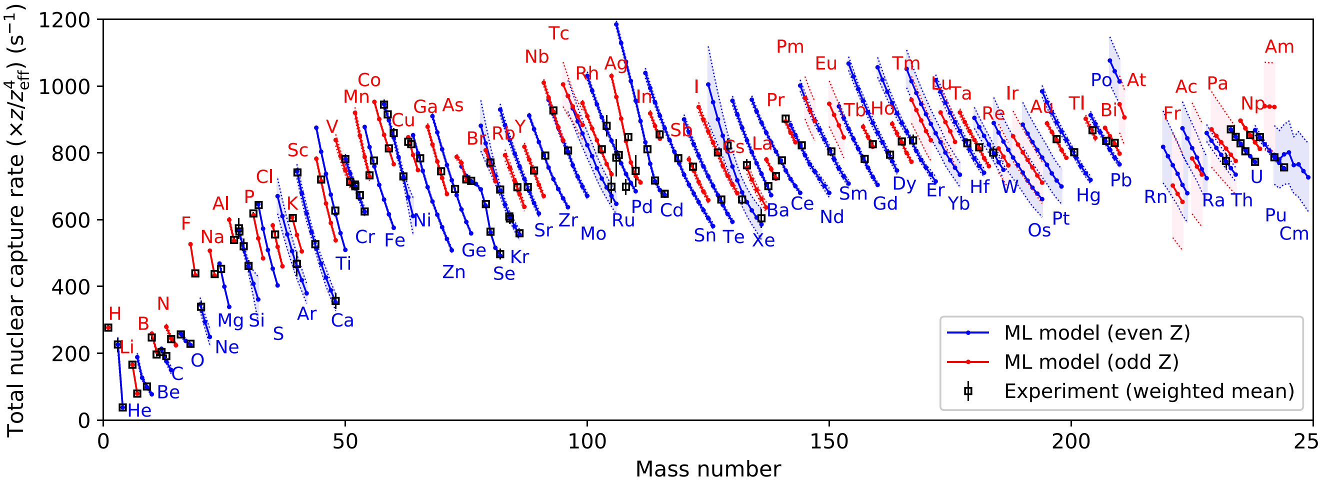

FIG. 6. Total nuclear capture rates for respective nuclei estimated by our ML model. The respective rates are multiplied by $z/z_{\rm eff}^4$ and shown in red for even-Z nuclei and in blue for odd-Z nuclei. The band widths represent 1σ uncertainties. The experimental data represent weighted means for each element. The estimated data can be found in the Supplemental Material [85].

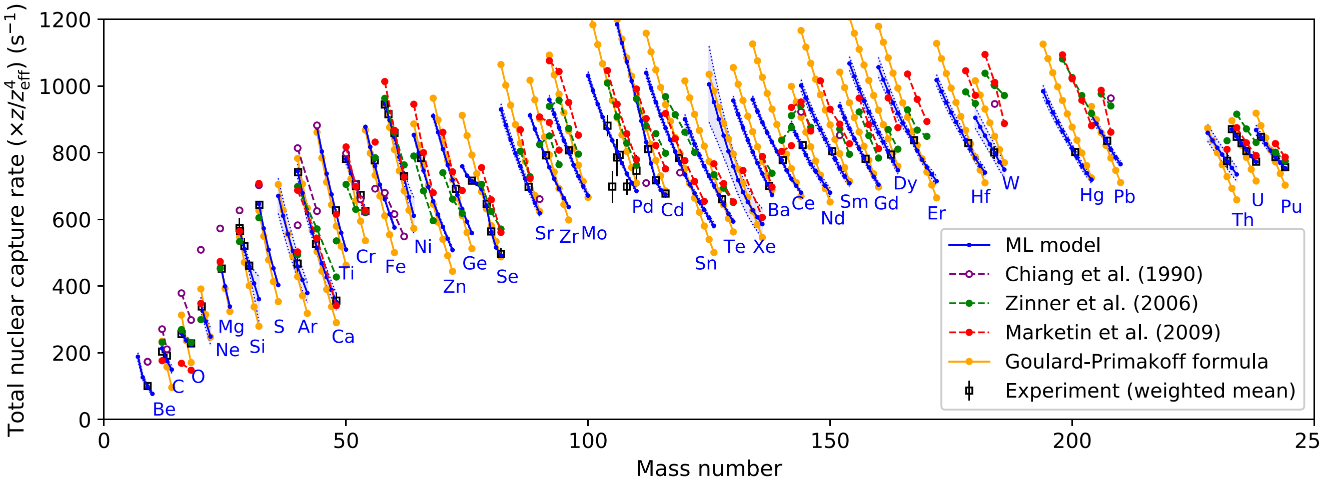

FIG. 7. Total nuclear capture rates for respective nuclei estimated by the four physics models (i.e., the Chiang model, the Zinner model, the Marketin model, and the Goulard-Primakoff formula) and our ML model. The respective rates are multiplied by $z/z_{\rm eff}^4$. The experimental data represent weighted means for each element.

C. Comparison with physics models

We compare the estimation results of our ML model with those of the Chiang, Zinner, Marketin models, as well as the Goulard-Primakoff formula, in Fig. 7. The calculation results for the Chiang, Zinner, and Marketin models were taken from Refs. [18,21,22], respectively. Since the Zinner and Marketin models, which are based on the RPA model, are only applicable to even-even nuclei, only the rates for even-Z nuclei are displayed. To capture the differences, we further plot the deviations from our ML model for the three models in Fig. 8.

While the Goulard-Primakoff formula predicts a structured relationship between the rates and A and Z numbers, the ML model reveals a more complex pattern. In particular, as also indicated in Fig. 5, Zinatulina's data for Se and Cd deviates noticeably from the Goulard-Primakoff formula's predictions. This suggests that additional variables or factors should be incorporated into the formula for more accurate predictions.

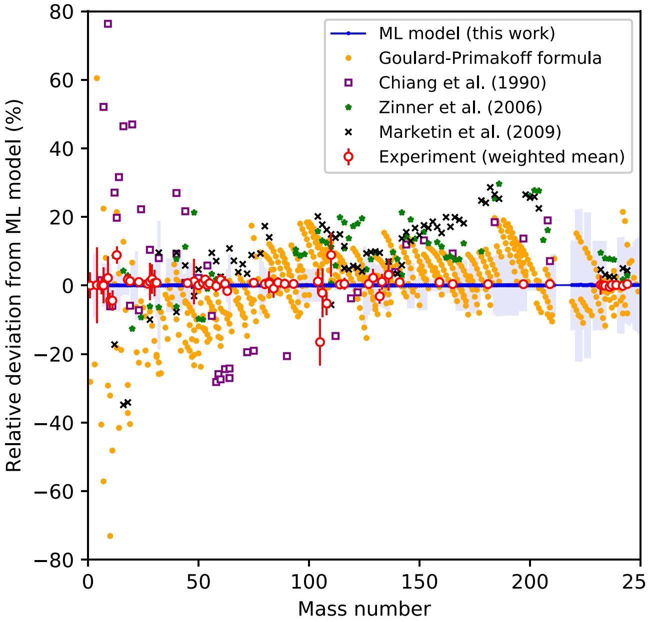

FIG. 8. Relative deviation from our ML model. The band widths and error bars represent 1σ uncertainties.

The remaining three physics models aim to explain the trend of the total nuclear capture rates for A and Z through their respective theoretical approximations. However, there are significant differences between the analytical and experimental values that exceed the measurement uncertainty. The primary difference between the Zinner and Marketin models lies in whether they incorporate a microscopic approach based on relativistic energy density functionals. However, both models consistently overestimate the total nuclear capture rates, particularly for medium and heavy nuclei, suggesting the need to incorporate additional theoretical refinements, such as accounting for more many-body correlations in the RPA model. Additionally, Zinner's and Marketin's RPA models exhibit a non-monotonic trend for certain nuclei (see Zr, Mo, Ce, and Nd in Fig. 5), while all current experimental results demonstrate monotonic decrease for each Z (e.g., Si, Cr, Ni, U, Pu). Although the Pd case appears to exhibit non-monotonic behavior, it is not possible to ascertain this due to significant measurement uncertainty.

We further evaluated the performance of our ML model and the three physics models for isotopic capture rates using the following metrics: χ^2/n, root mean squared error (RMSE), and root mean squared logarithmic error (RMSLE). These metrics are defined as follows:

$$\chi^2/n \equiv \frac{1}{n}\sum_{i=1}^{n}\frac{(\lambda_i - \lambda_{{\rm e},i})^2}{(\Delta\lambda_i)^2 + (\Delta\lambda_{{\rm e},i})^2}, \tag{25}$$

$$\text{RMSE} \equiv \sqrt{\frac{1}{n}\sum_{i=1}^{n}(\lambda_i - \lambda_{{\rm e},i})^2}, \tag{26}$$

$$\text{RMSLE} \equiv \sqrt{\frac{1}{n}\sum_{i=1}^{n}[\ln{(1+\lambda_i)} - \ln{(1+\lambda_{{\rm e},i})}]^2}, \tag{27}$$

TABLE III. Model performances of the ML and physics models.

	ML model	Goulard-Primakoff	Chiang *et al.*	Zinner *et al.*	Marketin *et al.*
n	65	65	21	17	25
χ^2/n	0.548	340	259	121	428
RMSE	0.256	0.614	0.484	0.868	0.886
RMSLE	0.011	0.032	0.031	0.034	0.036

where λ_i denotes the ith total nuclear capture rate in μs^{-1} estimated by the ML and physics models, $\Delta\lambda_i$ represents its 1σ uncertainty, which is applied only for the ML model, $\lambda_{e,i}$ and $\Delta\lambda_{e,i}$ are the corresponding experimental values and their uncertainties, and n is the number of experimental values that can be compared to the estimated values.

Table III summarizes the evaluated model performance. Of the three metrics, the closer χ^2/n approaches one, and the smaller the values of RMSE and RMSLE, the better the estimation performance. These metrics cannot be ranked exactly because they depend on the quantity and type of data being compared. However, the results show that the ML model outperforms the other models in terms of accuracy and comprehensiveness. While the Goulard-Primakoff formula can compute the rates comprehensively, the other physics models are less comprehensive; the Chiang model could potentially be comprehensive, but its accuracy remains uncertain due to the limited data available.

D. Toward further improvement

Figure 9 compares the total nuclear capture rates of Ca and Se isotopes with and without the inclusion of data from their respective isotopic training sets shown in Table II. For Ca, the estimates remain nearly unchanged and can be accurately predicted regardless of the inclusion of isotopic data. This suggests that, even without training data for $^{43.8}$Ca and ^{48}Ca, the slope of the capture rate with respect to ν (or A) derived from the Goulard-Primakoff formula is effectively improved by data for targets other than Ca. In contrast, for Se, the ML model overestimates the experimental values for ^{76}Se, ^{80}Se, and ^{82}Se when data for these isotopes are excluded. This suggests that the experiment by Zinatulina *et al.* [76] plays a significant role in the predictions for Se isotopes.

It should be noted, however, that the differential coefficient for Se, as defined in Fig. 5, is significantly larger than that predicted by the Goulard-Primakoff formula, and the trends in total nuclear capture rates for this element differ from those of other elements (see Fig. 6). The data for Se [76], Cd, [76], Pd [78], and Ca [35,75] isotopes were obtained from experiments measuring emitted γ rays after muon capture. This method of data acquisition differs from that used in experiments measuring muon-decay electrons. As shown in Fig. 5, these elements tend to exhibit steeper slopes except Ca, and the values derived from γ-ray measurements may differ from those obtained via muon-decay electron measurements. To address these discrepancies, further investigation into the differences between these measurement methods is required.

Furthermore, the Goulard-Primakoff formula suggests that total nuclear capture rates decrease smoothly as neutron

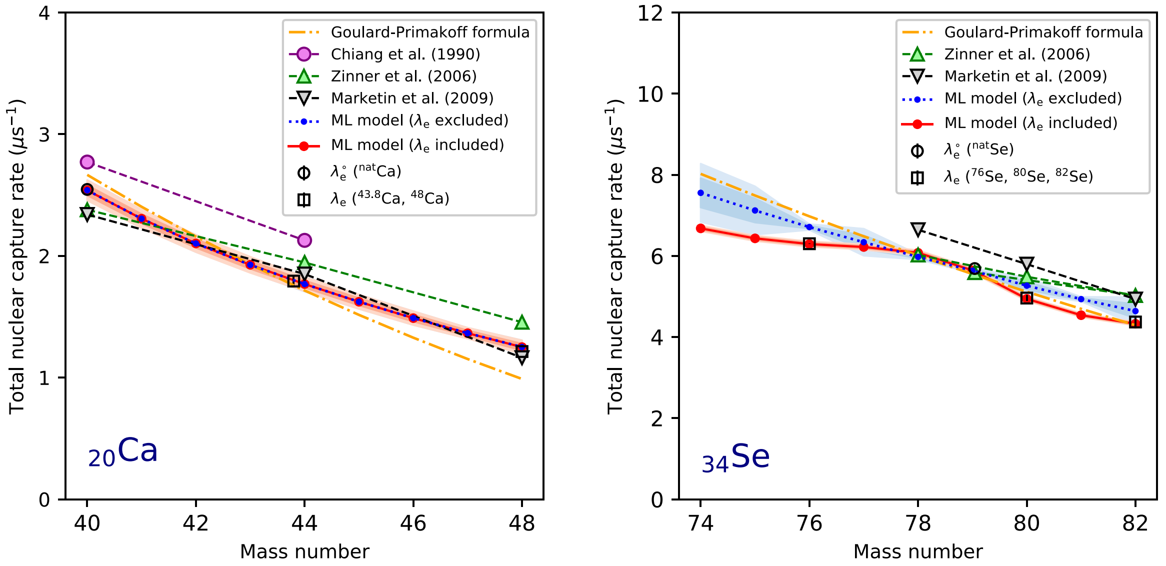

FIG. 9. Total nuclear capture rates for Ca (left) and Se (right) isotopes. The orange lines represent calculations using the Goulard-Primakoff formula. The blue lines with bands represent the GP-2 predictions, where isotopic experimental data are excluded from the training set in GP-1. The red lines with bands represent the GP-2 estimations, where all experimental data are included in the training set in GP-1. The darker and lighter colored band widths represent 1σ and 2σ uncertainties, respectively.

numbers increase for a given element, and experimental results thus far generally support this trend. However, the lack of experimental data prevents us from confirming the characteristic structure predicted by the Zinner and Marketin models for elements such as Zr, Mo, Ce, and Nd (see Fig. 7). Therefore, conducting experiments focused on these elements, or on elements with many stable isotopes, such as Sn and Pb, could help validate both the Goulard-Primakoff formula and the approximations underlying the RPA model.

IV. CONCLUSION

A comprehensive ML model using GP regression has been developed to estimate the total nuclear capture rate of negative muons. This model outperforms four existing physics models in terms of accuracy. We believe that the estimates in this study currently represent the most reliable values. Therefore, it is recommended that applications and simulations related to muon nuclear capture use the values provided by our ML model, rather than those derived solely from physics models. The estimates generated here will be incorporated into muon nuclear data and applied across various research fields. However, it should be noted that the data have room for improvement and would change with new experimental data or advancements in physics models. Future work should focus on measuring total nuclear capture rates for as many isotopes as possible, across a wide range of elements. This would not only improve the accuracy of our ML model but also enhance our theoretical understanding of the physics of muon-induced reactions.

ACKNOWLEDGMENTS

The authors thank S. Kawase, F. Minato and Y. Watanabe of Kyushu University for valuable comments on this work. R.M. is supported by the Force-front Physics and Mathematics Program in Drive Transformation (FoPM), a World-leading Innovative Graduate Study (WINGS) program, and the JSR Fellowship from the University of Tokyo.

DATA AVAILABILITY

The data that support the findings of this article are openly available [85].

[1] S. Charalambus, Nuclear transmutation by negative stopped muons and the activity induced by the cosmic-ray muons, Nucl. Phys. A **166**, 145 (1971).

[2] J. Stone, J. Evans, L. Fifield, G. Allan, and R. Cresswell, Cosmogenic chlorine-36 production in calcite by muons, Geochim. Cosmochim. Acta **62**, 433 (1998).

[3] H. Araújo, V. A. Kudryavtsev, N. J. C. Spooner, and T. J. Sumner, Muon-induced neutron production and detection with GEANT4 and FLUKA, Nucl. Instrum. Methods Phys. Res. Sect. A **545**, 398 (2005).

[4] S. Abe and T. Sato, Feasibility study of nuclear transmutation by negative muon capture reaction using the PHITS code, EPJ Web Conf. **122**, 04002 (2016).

[5] G. Balco, Production rate calculations for cosmic-ray-muon-produced ^{10}Be and ^{26}Al benchmarked against geological calibration data, Quat. Geochronol. **39**, 150 (2017).

[6] R. Saldanha, R. Thomas, R. H. M. Tsang *et al.*, Cosmogenic activation of silicon, Phys. Rev. D **102**, 102006 (2020).

[7] T. Kato, M. Tampo, S. Takeshita *et al.*, Muon-induced single-event upsets in 20-nm SRAMS: Comparative characterization with neutrons and alpha particles, IEEE Trans. Nucl. Sci. **68**, 1436 (2021).

[8] M. McEwen, L. Faoro, K. Arya *et al.*, Resolving catastrophic error bursts from cosmic rays in large arrays of superconducting qubits, Nat. Phys. **18**, 107 (2022).

[9] S. Musy and R. Purtschert, Reviewing ^{39}Ar and ^{37}Ar underground production in shallow depths with implications for groundwater dating, Sci. Total Environ. **884**, 163868 (2023).

[10] M. Niikura, S. Abe, S. Kawase *et al.*, *Muon Nuclear Data*, JAEA-Conf. 2024-002 (Japan Atomic Energy Agency, 2024), pp. 29–34.

[11] B. Goulard and H. Primakoff, Nuclear muon-capture sum and mean nuclear excitation energies, Phys. Rev. C **10**, 2034 (1974).

[12] T. Sato, Y. Iwamoto, S. Hashimoto *et al.*, Recent improvements of the particle and heavy ion transport code system–PHITS version 3.33, J. Nucl. Sci. Technol. **59**, 1004 (2023).

[13] G. Battistoni, T. Boehlen, F. Cerutti *et al.*, Overview of the FLUKA code, Ann. Nucl. Energy **82**, 10 (2015).

[14] J. Allison, K. Amako, J. Apostolakis *et al.*, Recent developments in Geant4, Nucl. Instrum. Methods Phys. Res. Sect. A **835**, 186 (2016).

[15] D. F. Measday, The nuclear physics of muon capture, Phys. Rep. **354**, 243 (2001).

[16] H. Primakoff, Theory of muon capture, Rev. Mod. Phys. **31**, 802 (1959).

[17] N. Van Giai, N. Auerbach, and A. Z. Mekjian, Self-consistent random-phase-approximation calculations of muon capture rates, Phys. Rev. Lett. **46**, 1444 (1981).

[18] H. C. Chiang, E. Oset, and P. Fernández De Córdoba, Muon capture revisited, Nucl. Phys. A **510**, 591 (1990).

[19] E. Kolbe, K. Langanke, and P. Vogel, Muon capture on nuclei with $Z > A$, random phase approximation, and in-medium value of the axial-vector coupling constant, Phys. Rev. C **62**, 055502 (2000).

[20] J. Nieves, J. E. Amaro, and M. Valverde, Inclusive quasielastic charged-current neutrino-nucleus reactions, Phys. Rev. C **70**, 055503 (2004).

[21] N. T. Zinner, K. Langanke, and P. Vogel, Muon capture on nuclei: Random phase approximation evaluation versus data for $6 \leqslant Z \leqslant 94$ nuclei, Phys. Rev. C **74**, 024326 (2006).

[22] T. Marketin, N. Paar, T. Nikšić, and D. Vretenar, Relativistic quasiparticle random-phase approximation calculation of total muon capture rates, Phys. Rev. C **79**, 054323 (2009).

[23] L. Jokiniemi, P. Navrátil, J. Kotila, and K. Kravvaris, Muon capture on ^{6}Li, ^{12}C, and ^{16}O from *ab initio* nuclear theory, Phys. Rev. C **109**, 065501 (2024).

[24] A. Boehnlein, M. Diefenthaler, N. Sato *et al.*, *Colloquium:* Machine learning in nuclear physics, Rev. Mod. Phys. **94**, 031003 (2022).

[25] H. Iwamoto, S. I. Meigo, and K. Sugihara, Comprehensive estimation of nuclide production cross sections using a phenomenological approach, Phys. Rev. C **109**, 054610 (2024).

[26] H. Iwamoto, O. Iwamoto, and S. Kunieda, G-HyND: A hybrid nuclear data estimator with Gaussian processes, J. Nucl. Sci. Technol. **59**, 334 (2022).

[27] H. Iwamoto, Generation of nuclear data using Gaussian process regression, J. Nucl. Sci. Technol. **57**, 932 (2020).

[28] J. C. Sens, Capture of negative muons by nuclei, Phys. Rev. **113**, 679 (1959).

[29] F. R. Stannard, Total absorption rate of muons in carbon, Phys. Rev. Lett. **4**, 523 (1960).

[30] R. A. Reiter, T. A. Romanowski, R. B. Sutton, and B. G. Chidley, Precise measurements of the mean lives of μ^+ and μ^- mesons in carbon, Phys. Rev. Lett. **5**, 22 (1960).

[31] W. J. Bertram, R. A. Reiter, T. A. Romanowski, and R. B. Sutton, Observation of the "isotope effect" in the nuclear capture of negative muons by chlorine, Phys. Rev. Lett. **5**, 61 (1960).

[32] J. L. Lathrop, R. A. Lundy, V. L. Telegdi *et al.*, Measurements of muon disappearance rates vs time in C, Mg, Al, Si, and P, Phys. Rev. Lett. **7**, 107 (1961).

[33] I. M. Blair, H. Muirhead, T. Woodhead, and J. N. Woulds, The effect of atomic binding on the decay rate of negative muons, Proc. Phys. Soc. **80**, 938 (1962).

[34] M. Eckhause, T. Filippas, R. Sutton *et al.*, Experimental tests of the Fermi-Teller ⟨Z-law⟩, Il Nuovo Cimento **24**, 666 (1962).

[35] W. A. Cramer, V. L. Telegdi, R. Winston, and R. A. Lundy, Muon capture rates for ^{44}Ca and ^{40}Ca, Nuovo Cimento **24**, 546 (1962).

[36] T. Filippas, P. Palit, R. Siegel, and R. Welsh, Negative muon capture rates in high-Z elements, Phys. Lett. **6**, 118 (1963).

[37] M. Eckhause, T. A. Filippas, R. B. Sutton, and R. E. Welsh, Measurements of negative-muon lifetimes in light isotopes, Phys. Rev. **132**, 422 (1963).

[38] J. L. Rosen, E. W. Anderson, E. J. Bleser *et al.*, Muon capture in neon, Phys. Rev. **132**, 2691 (1963).

[39] G. Conforto, C. Rubbia, and E. Zavattini, Nuclear capture of negative muons from neon, Phys. Lett. **4**, 239 (1963).

[40] J. A. Diaz, S. N. Kaplan, and R. V. Pyle, Nuclear fission induced by radiationless transitions in the MU-mesonic atoms Th^{232}, U^{235} and U^{238}, Nucl. Phys. **40**, 54 (1963).

[41] R. Winston, Observable hyperfine effects in muon capture by complex nuclei, Phys. Rev. **129**, 2766 (1963).

[42] R. Bizzarri, E. Di Capua, U. Dore *et al.*, Experimental determination of the total capture rate of negative muons in ^{4}He, Nuovo Cimento **33**, 1497 (1964).

[43] J. Barlow, J. Sens, P. Duke, and M. Kemp, Evidence for giant resonance excitation induced by the capture of muons in O^{16}, Phys. Lett. **9**, 84 (1964).

[44] M. Eckhause, R. Siegel, R. Welsh, and T. Filippas, Muon capture rates in complex nuclei, Nucl. Phys. **81**, 575 (1966).

[45] V. Bobrov, V. Varlamov, Y. Grashin *et al.*, Capture of negative muons in pure isotopes of Ni and Cr, Yad. Fiz. **4**, 75 (1966); V. Varlamov, Y. Grashin *et al.*, Sov. J. Nucl. Phys. **4**, 53 (1967).

[46] V. Cojocaru, L. Marinescu, M. Petrascu *et al.*, Fission by a radiationless transition in the μ mesonic atom ^{239}Pu, Phys. Lett. **20**, 53 (1966).

[47] M. M. Block, T. Kikuchi, D. Koetke *et al.*, The total capture rate of negative muons in ^{4}He, Nuovo Cimento A **55**, 501 (1968).

[48] B. Budick, S. C. Cheng, E. R. Macagno *et al.*, Muon- and pion-induced fission of uranium isotopes, Phys. Rev. Lett. **24**, 604 (1970).

[49] H. Povel, H. Koch, W. Hamilton *et al.*, Muon capture probability in isotopes of bromine, Phys. Lett. B **33**, 620 (1970).

[50] L. DiLella, I. Hammerman, and L. M. Rosenstein, Photon asymmetry for radiative μ capture in calcium, Phys. Rev. Lett. **27**, 830 (1971).

[51] A. Buta, D. Dorcioman, and N. Grama, Mechanisms of ^{239}Pu fission by muons, Rev. Roum. Phys. **16**, 215 (1971).

[52] A. Bertin, A. Vitale, and A. Placci, Nuclear capture of muons in argon and neon, Phys. Rev. A **7**, 2214 (1973).

[53] D. Chultem, V. Cojocaru, D. Gansorig *et al.*, Fission of ^{232}Th, ^{238}U and ^{235}U induced by negative muons, Nucl. Phys. A **247**, 452 (1975).

[54] B. Aleksandrov, G. Buklanov, W. Fromm *et al.*, Muon induced fission of ^{237}Np, ^{239}Pu and ^{242}Pu, Phys. Lett. B **57**, 238 (1975).

[55] Y. K. Gavrilov, K. S. Chwan, V. Cojocaru *et al.*, Probability of fission of ^{232}Th by μ^- mesons, Yad. Fiz. **24**, 241 (1976); Sov. J. Nucl. Phys. **24**, 125 (1976).

[56] R. D. Hart, C. R. Cox, G. W. Dobson, M. Eckhause, J. R. Kane, M. S. Pandey, A. M. Rushton, R. T. Siegel, and R. E. Welsh, Radiative muon capture in calcium, Phys. Rev. Lett. **39**, 399 (1977).

[57] G. Bardin, J. Duclos, J. Joseph *et al.*, Total muon capture rate in ^{6}Li and ^{7}Li, Phys. Lett. B **79**, 52 (1978).

[58] H. W. Reist, A. Grütter, H. R. von Gunten, and D. Jost, Fission probabilities and time distributions in μ-induced fission of ^{232}Th, ^{233}U, ^{235}U, and ^{238}U, in *Proceedings of the International Symposium on Physics and Chemistry of Fission* (International Atomic Energy Agency, Vienna, 1979), pp. 13–32.

[59] W. U. Schröder, W. W. Wilcke, M. W. Johnson, D. Hilscher, J. R. Huizenga, J. C. Browne, and D. G. Perry, Evidence for atomic muon capture by fragments from prompt fission of muonic ^{237}Np, ^{239}Pu, and ^{242}Pu, Phys. Rev. Lett. **43**, 672 (1979).

[60] G. Carboni, G. Gorini, G. Torelli *et al.*, Muonic x-rays and muon capture in low-pressure argon, Phys. Lett. B **96**, 206 (1980).

[61] D. Ganzorig, P. Hansen, T. Johansson *et al.*, Fission of ^{232}Th and ^{238}U in the interaction with negative muons, Nucl. Phys. A **350**, 278 (1980).

[62] G. Bardin, J. Duclos, A. Magnon *et al.*, A novel measurement of the muon capture rate in liquid hydrogen by the lifetime technique, Nucl. Phys. A **352**, 365 (1981).

[63] J. Martino, Mesure du taux de capture mu dans l'hydrogène liquide par la méthode du temps de vie, Ph.D. thesis, Universite de Paris-Sud, Orsay, 1982.

[64] P. David, J. Hartfiel, H. Janszen *et al.*, Total kinetic energy release and mass distributions in prompt and delayed muon induced fission of ^{238}U, Phys. Lett. B **124**, 161 (1983).

[65] M. Cargnelli, W. H. Breunlich, H. Fuhrmann *et al.*, New experimental results on hyperfine transitions in muonic hydrogen isotopes, in *Proceedings of 10th International Conference on Particles and Nuclei (PANIC 84), Paper K6* (North Holland Physics Publication, Heidelberg, 1984).

[66] J. Martino, A new measurement of muon capture in liquid deuterium, Czech. J. Phys. B **36**, 368 (1986).

[67] K. Ishida, J. Brewer, T. Matsuzaki *et al.*, Pulsed μ^- SR measurement of negative muon depolarization in muonic ^{13}C and ^{14}N, Phys. Lett. B **167**, 31 (1986).

[68] S. Ahmad, O. Häusser, J. A. Macdonald *et al.*, Muon-induced fission in ^{235}U and ^{238}U, Can. J. Phys. **64**, 665 (1986).

[69] T. Suzuki, D. F. Measday, and J. P. Roalsvig, Total nuclear capture rates for negative muons, Phys. Rev. C **35**, 2212 (1987).

[70] S. Ahmad, G. A. Beer, B. H. Olaniyi *et al.*, Search for the shape isomeric gamma decay in muonic uranium, Can. J. Phys. **65**, 753 (1987).

[71] P. David, H. Hänscheid, J. Hartfiel *et al.*, The study of prompt delayed muon induced fission, Z. Phys. A **330**, 397 (1988).

[72] H. Hänscheid, P. David, J. Konijn *et al.*, Muon capture rates in ^{233}U, ^{234}U, ^{235}U, ^{236}U, ^{238}U, and ^{237}Np, Z. Phys. A **335**, 1 (1990).

[73] T. N. Mamedov, V. G. Grebinnik, V. A. Zhukov *et al.*, Measurement of the rate of nuclear capture of negative muons in the isotopes ^{84}Kr and ^{136}Xe, JETP Lett. **67**, 318 (1998).

[74] T. N. Mamedov, V. G. Grebinnik, and K. I. Gritsai, Isotope effect in nuclear capture of negative muons in xenon, JETP Lett. **71**, 451 (2000).

[75] H. O. U. Fynbo, V. Egorov, and V. Brudanin, The muon capture rate of ^{48}Ca, Nucl. Phys. A **724**, 493 (2003).

[76] D. Zinatulina, V. Brudanin, V. Egorov, C. Petitjean, M. Shirchenko, J. Suhonen, and I. Yutlandov, Ordinary muon capture studies for the matrix elements in $\beta\beta$ decay, Phys. Rev. C **99**, 024327 (2019).

[77] V. Belov, K. Gusev, I. Zhitnikov *et al.*, Total capture rate of negative muons in ^{24}Mg, Phys. Part. Nuclei Lett. **19**, 221 (2022).

[78] T. Y. Saito, M. Niikura, T. Matsuzaki, H. Sakurai, M. Igashira, H. Imao, K. Ishida, T. Katabuchi, Y. Kawashima, M. K. Kubo, Y. Miyake, Y. Mori, K. Ninomiya, A. Sato, K. Shimomura, P. Strasser, A. Taniguchi, D. Tomono, and Y. Watanabe, Muonic X-ray measurement for the nuclear charge distribution: The case of stable palladium isotopes, Phys. Rev. C **111**, 034313 (2025).

[79] R. Mizuno, S. Akamatsu, T. Fujiie *et al.*, Lifetime measurement of the muonic atom of enriched Si isotopes, arXiv:2501.05897.

[80] Y. Miyake, K. Shimomura, N. Kawamura *et al.*, J-PARC muon facility, MUSE, Phys. Procedia **30**, 46 (2012).

[81] S. F. Mughabghab, *Atlas of Neutron Resonances: Resonance Properties and Thermal Cross Sections Z = 1–60*, 6th ed. (Elsevier, Amsterdam, 2018), Vol. 1.

[82] H. Harada, P. Schillebeeckx, O. Cabellos *et al.*, *Improving Nuclear Data Accuracy of the* ^{241}Am *Capture Cross-Section, NEA-NSC-R–2020-2* (Nuclear Energy Agency of the OECD, 2020).

[83] C. Zhu, R. H. Byrd, P. Lu *et al.*, Algorithm 778: L-BFGS-B: Fortran subroutines for large-scale bound-constrained optimization, ACM Trans. Math. Softw. **23**, 550 (1997).

[84] K. W. Ford and J. G. Wills, Calculated properties of μ-metsonic atoms, Nucl. Phys. **35**, 295 (1962).

[85] See Supplemental Material at http://link.aps.org/supplemental/10.1103/PhysRevC.111.034614 for the dataset of the total nuclear capture rates generated by our ML model.